Eur. Phys. J. C (2026) 86:119
https://doi.org/10.1140/epjc/s10052-026-15344-5

THE EUROPEAN PHYSICAL JOURNAL C

Regular Article - Theoretical Physics

Periodic orbits and quasinormal modes of a black hole surrounded by King dark matter halo

Hassan Hassanabadi[1,2,a], **Jing Zhang**[3,b], **Dhruba Jyoti Gogoi**[4,c], **Farokhnaz Hosseinifar**[5,d], **Soroush Zare**[1,6,e]

[1] Department of Physics, Faculty of Science, University of Hradec Králové, Rokitanského 62, 500 03 Hradec Králové, Czechia
[2] Department of Physics and Electronics, Khazar University, 41 Mahsati Str, 1096 Baku, Azerbaijan
[3] Purple Mountain Observatory, Chinese Academy of Sciences, Nanjing 210023, China
[4] Department of Physics, Madhabdev University, Narayanpur, Lakhimpur 784164, Assam, India
[5] Center for Theoretical Physics, Khazar University, 41 Mehseti Street, AZ1096 Baku, Azerbaijan
[6] Helsinki Institute of Physics, University of Helsinki, P.O. Box 64, 00014 Helsinki, Finland

Received: 2 November 2025 / Accepted: 16 January 2026

Abstract We examine the Hawking radiation sparsity and quasinormal mode (QNM) spectra of a Schwarzschild black hole surrounded by the King dark matter distribution. The modified metric, derived from the King density profile, yields altered expressions for the lapse function, mass, and Hawking temperature. The presence of dark matter reduces the Hawking temperature, indicating suppressed thermal emission. Analysis of radiation sparsity reveals its dependence on the horizon radius, with larger scale radius R and central density ρ_0 enhancing sparsity compared to the constant value in the Schwarzschild case. The photon sphere and shadow radius increase with R and ρ_0, suggesting enlarged black hole shadows under dark matter influence. Hawking emission rates exhibit a downward shift in both peak intensity and frequency. The QNM spectra, obtained via the Mashhoon and 3rd-order Wentzel–Kramers–Brillouin (WKB) methods, show that both the oscillation frequencies and damping or decay rate decrease with the dark matter parameter $\alpha = 8\pi\rho_0 R^2$. This study also examines how King dark matter halo affects periodic particle motion around a black hole, showing that it alters orbital stability and enhances precession, leading to transitions from bound to unbound motion. These results collectively demonstrate that King dark matter substantially modifies the thermodynamic and dynamical properties of black holes, offering potential observational imprints in black hole shadow and gravitational wave studies.

1 Introduction

In the realm of cosmology, a pivotal area of exploration is the study of black holes and the complex interactions of the surrounding matter [1–4]. The concept of dark matter has its roots in early 20th-century astrophysics, beginning with Fritz Zwicky's observations of the Coma Cluster in 1933. He noted that the visible mass of galaxies could not account for the high velocities of galaxies within the cluster, suggesting the presence of unseen mass[5,6]. This idea was largely overlooked for several decades, until Vera Rubin's groundbreaking work in the 1970 s on galactic rotation curves provided compelling evidence for dark matter's existence [7,8]. Rubin's findings indicated that the outer regions of galaxies were rotating at speeds that could not be explained solely by the visible matter present.

Throughout the latter half of the 20th century, the acceptance of dark matter grew as more observational evidence emerged, including studies of gravitational lensing and cosmic microwave background radiation [9–11]. Despite the strong evidence supporting its existence, the precise nature of dark matter remains elusive, leading to ongoing research and theoretical developments in the field [12–14]. The historical journey of dark matter reflects the evolving understanding of the universe and highlights the complexities involved in unraveling its mysteries [15].

[a] e-mail: hha1349@gmail.com (corresponding author)
[b] e-mail: jingzhang@pmo.ac.cn
[c] e-mail: moloydhruba@yahoo.in
[d] e-mail: f.hoseinifar94@gmail.com
[e] e-mail: soroushzrg@gmail.com

Published online: 05 February 2026

The concept of QNMs has emerged as a cornerstone in the study of black hole perturbation theory and gravitational wave astrophysics. QNMs refer to a discrete set of complex frequencies that characterize the damped oscillations of perturbed compact objects, such as black holes and neutron stars, under external or internal disturbances [16–18]. When a black hole is perturbed – by, for instance, an infalling particle or a surrounding field – the resulting perturbations do not persist indefinitely. Instead, they decay over time through the emission of gravitational waves, the spectral properties of which are encoded in the QNM frequencies. The real part of the frequency corresponds to the oscillation frequency of the emitted wave, whereas the imaginary part determines the damping rate or decay timescale of the oscillation.

From a physical perspective, QNMs act as the "fingerprints" of black holes, since their frequencies depend solely on the intrinsic parameters of the background spacetime – namely the mass, charge, and angular momentum – and are independent of the initial perturbation [18]. This property renders QNMs a powerful diagnostic tool for testing the no-hair theorem and probing the nature of gravity in strong-field regimes. In recent years, with the direct detection of gravitational waves by the LIGO–Virgo collaboration, the study of QNMs has gained renewed importance as it allows one to extract fundamental information about astrophysical black holes and to constrain deviations from General Relativity.

Numerous investigations have been carried out by using different methods to understand how quasinormal spectra are modified in various extended and alternative theories of gravity [19–39]. For instance, in Lorentz-violating frameworks such as Bumblebee gravity, the influence of symmetry breaking on QNM frequencies has been systematically explored [40], revealing that Lorentz violation can lead to shifts in both the oscillation and damping rates. QNMs of d-dimensional regular black holes have been investigated in Ref. [41]. QNMs of black holes embedded in halos of matter have been investigated in Ref. [42]. These investigations show that QNMs play a very important role in understanding the characteristics of a black hole spacetime in different theories of gravity in different environments.

Beyond their theoretical elegance, QNMs also serve as a crucial link between black hole thermodynamics, quantum gravity effects, and observational astrophysics. The spectral structure of QNMs encodes information about horizon dynamics, potential barriers, and the causal structure of spacetime, while their damping behavior reflects the irreversible nature of black hole relaxation processes. Therefore, an in-depth analysis of QNMs not only enhances our understanding of black hole physics but also provides an effective framework for probing dark matter interactions, horizon-scale modifications, and emergent quantum gravitational phenomena in the strong-field regime.

Extreme mass–ratio inspirals are essential for future gravitational wave astronomy, particularly with space-based detectors [43,44]. The unique properties of periodic orbits generated in strong gravitational fields can be used to distinguish different spacetimes, which has made them attract considerable attention in recent years. A periodic orbit refers to the orbit in which the particle can exactly go back to its initial position after a finite amount of time. In the strong gravitational field, the particles in a periodic orbit will zoom in a quasi-elliptical orbit near the black hole and loop it several times before quickly moving away, forming the zoom-whirl patterns [45–48]. A characteristic number p— defined as the ratio of the average angular frequency to the radial frequency per radial cycle— can be used to describe this unique strong-field feature [49]. Hence, a rational p implies that the particle will exactly revisit its starting location after a finite period and trace a perfect periodic orbit. Conversely, when p is irrational, the particle follows a precessing orbit; however, such an orbit can be closely approximated by a nearby periodic one, as rational numbers are dense in the real number field. So far, the periodic orbits around the Schwarzschild black hole [49], the Kerr black hole [50–55], black holes surrounded by dark matters [56,57], and other black holes [58–83] or binary black holes [84,85] have been thoroughly studied.

In this study, we delve into the properties of the Schwarzschild black hole, specifically focusing on its interaction with King dark matter. We begin in Sect. 2 by introducing the black hole metric and examining the characteristics of Hawking radiation, particularly its sparsity. Following this, Sect. 3 is dedicated to a detailed analysis of the emission rate associated with this black hole. In Sect. 4, we explore QNMs through two distinct methodologies, providing a comprehensive comparison of the results. Section 5 shifts our focus to the time-domain profile, offering insights into its dynamic behavior. Subsequently, in Sect. 6, we calculate the grey-body factors and partial absorption cross section, emphasizing their significance in the context of black hole thermodynamics. Section 7 investigates periodic motion, shedding light on the stability and oscillatory patterns of the system. Finally, in Sect. 8, we present a synthesis of our findings, highlighting the implications of our research and potential avenues for future exploration.

2 Hawking radiation sparsity of a Schwarzschild black hole influenced by King dark matter

In this work, we utilize the solution of the black hole elegantly derived in Ref. [86]. The authors considered a spherically symmetric geometry

$$ds^2 = -f(r)dt^2 + \frac{dr^2}{f(r)} + h(r)(d\theta^2 + \sin^2\theta d\phi^2), \qquad (1)$$

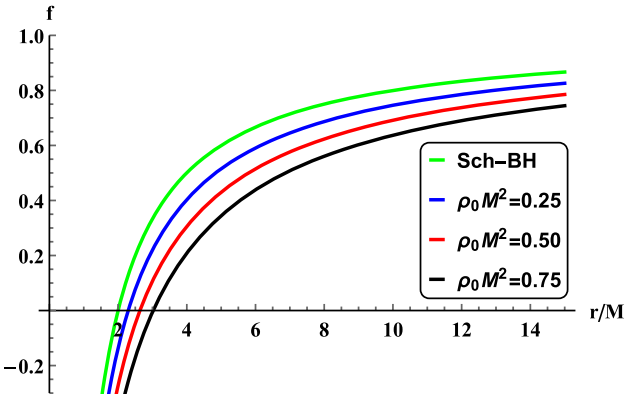

Fig. 1 The illustration of $f(r)$ as function of r/M for $R/M = 0.3$

surrounded by King dark matter distribution with a density described by [87]

$$\rho(r) = \rho_0 \left(1 + \left(\frac{r}{R}\right)^2\right)^{-3/2}. \tag{2}$$

where R and ρ_0 refer to the scale radius and the central density, respectively. The computed the lapse function as follows [86]

$$f(r) = 1 - \frac{2M}{r} + \frac{8\pi\rho_0 R^3}{\sqrt{r^2+R^2}} + \frac{8\pi\rho_0 R^3}{r} \ln\left(\frac{\sqrt{r^2+R^2}-r}{R}\right),$$
$$h(r) = r^2. \tag{3}$$

When R or ρ_0 tends zero, this function reduces to the lapse function of Schwarzschild black hole. At horizon, this function becomes zero $f(r_h) = 0$, where r_h represents horizon radius. Figure 1 demonstrates the variation of $f(r)$ in terms of radius considering $R/M = 0.3$.

As shown, this function has only one root. Mass of the black hole as function of horizon radius is obtained from $f(r_h) = 0$ and reads

$$M(r_h) = \frac{r_h}{2} + \frac{4\pi\rho_0 r_h R^3}{\sqrt{r_h^2+R^2}} + 4\pi\rho_0 R^3 \ln\left(\frac{\sqrt{r_h^2+R^2}-r_h}{R}\right). \tag{4}$$

When the parameters R or ρ_0 tend toward zero, mass of the black hole in the presence of King dark matter of Eq. (4), approaches that of the Schwarzschild black hole.

Hawking temperature employing Eqs. (3) and (4) is given by [88,89]

$$T_{\rm H} = \frac{1}{4\pi r_h} - \frac{2\rho_0 r_h R^3}{\left(r_h^2+R^2\right)^{3/2}}, \tag{5}$$

In the limit as $R \to 0$ or $\rho_0 \to 0$, the second term in the Eq. (5) disappears, causing the Hawking temperature of the black hole influenced by King dark matter converge to the Hawking temperature of the Schwarzschild black hole.

2.1 Sparsity of Hawking radiation

Black hole radiation is not a continuous stream but a highly discrete and infrequent process, and because of it, we introduce a quantity named sparsity to describe its intense gravitational pull and energy. It describes how the emission of individual particles from a black hole is rare and widely separated in time compared to their characteristic wavelength or frequency. For understanding how information and energy are released from a black hole, it is crucial to know the sparsity in both quantum gravity and black hole thermodynamics. Sparsity has applications in the study of black hole evaporation, quantum field theory in curved spacetime. By analyzing the sparse nature of black hole emissions, it is understandable how microphysics governs event horizons and the possible quantum structure of spacetime itself. This quantity is obtained from [90–92]

$$\eta = \frac{C}{\tilde{g}}\left(\frac{\lambda_t^2}{\mathcal{A}_{\rm eff}}\right), \quad \lambda_t = \frac{2\pi}{T_{\rm H}}. \tag{6}$$

where the term $\mathcal{A}_{\rm eff} = (27/4)\mathcal{A}_{\rm BH}$ indicates the effective area of the black hole and equals $\mathcal{A}_{\rm eff} = 27\pi r_h^2$, and C and $\tilde{g}$ are dimensionless constant and the degeneracy factor, respectively. Thus Eq. (6) can be rewritten as

$$\eta = \frac{64\pi^3\left(r_h^2+R^2\right)^3}{27\left(\left(r_h^2+R^2\right)^{3/2} - 8\pi\rho_0 r_h^2 R^3\right)^2}. \tag{7}$$

The above expression converges to $64\pi^3/27$ as R (ρ_0) approaches zero, which corresponds to the sparsity of the Schwarzschild black hole. Figure 2 illustrates the variations of sparsity as a function of the horizon radius for different parameters.

The sparsity of the Schwarzschild black hole does not depend on the horizon radius; however, the presence of King dark matter modifies this quantity to become dependent on the horizon radius. Increasing the parameter R (ρ_0) results in an increase in the size of the sparsity. At a fixed horizon and R (ρ_0), increasing the parameter ρ_0 (R) also leads to an increase in sparsity size. As the horizon radius increases, the influence of the King dark matter parameters on sparsity diminishes, and for large horizon radii, the sparsity of the black hole in the presence of dark matter approaches that of the Schwarzschild black hole.

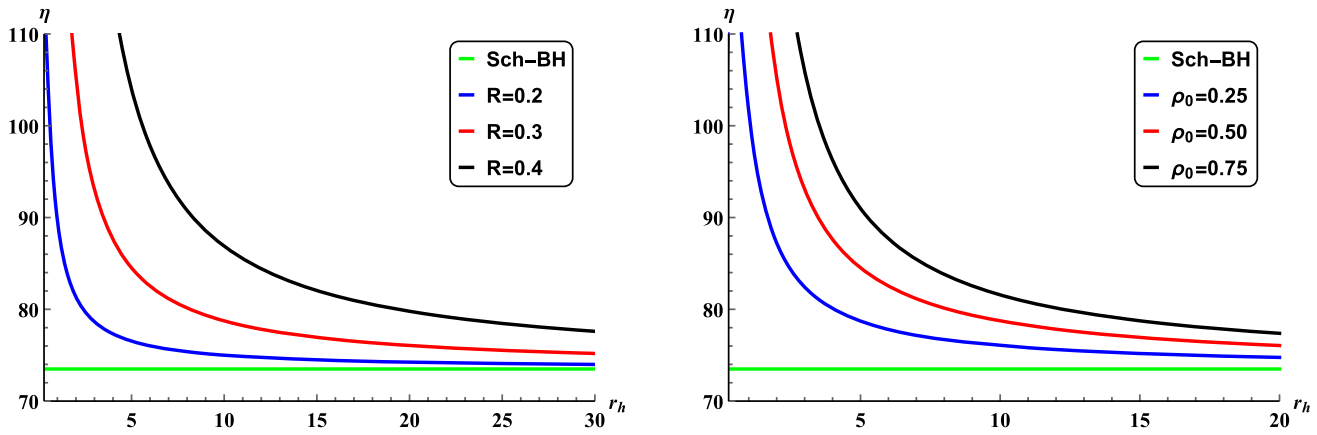

Fig. 2 Sparsity of Hawking radiation by varying r_h

3 Emission rate of a Schwarzschild black hole in presence of King dark matter

3.1 Photon sphere and shadow

For the spherically symmetric and static metric of form Eq. (1), the motion of massless particles can be described by using the Lagrangian $\mathcal{L} = (1/2)g_{\mu\nu}\dot{x}^\mu\dot{x}^\nu$ which is expressed as [93–95]

$$\mathcal{L}(x,\,\dot{x}) = \frac{1}{2}\left(-f(r)\dot{t}^2 + \frac{\dot{r}^2}{f(r)} + h(r)(\dot{\theta}^2 + \sin^2\theta\dot{\phi}^2)\right). \tag{8}$$

In the equatorial plane $\theta = \pi/2$. The motion of light is obtained by applying the Euler–Lagrange equation which is defined as [96]

$$\frac{d}{d\lambda}\left(\frac{\partial\mathcal{L}}{\partial\dot{x}^\mu}\right) - \frac{\partial\mathcal{L}}{\partial x^\mu} = 0, \tag{9}$$

to the Lagrangian of Eq. (8). For null geodesics, and by defining two constants of motion as

$$\epsilon = f(r)\dot{t}, \quad \ell = h(r)\dot{\phi}, \tag{10}$$

and doing some calculations, the orbit equation for lightlight geodesics is obtained as

$$\left(\frac{dr}{d\phi}\right)^2 = h(r)f(r)\left(\frac{h(r)}{f(r)}\frac{\epsilon^2}{\ell^2} - 1\right). \tag{11}$$

Considering the above equation, similar to the energy conservation law, an effective potential can be defined which is calculated from $(dr/d\phi)^2 + V_{\text{eff}}(r) = 0$. The circular orbits of this potential can be found by solving [97]

$$V_{\text{eff}}(r) = 0, \quad \text{and} \quad \partial_r V_{\text{eff}}(r) = 0. \tag{12}$$

The photon sphere of the black hole, which represents a critical region where light can orbit the black hole is located at the solutions of the above equation. Thus one can obtained that the photon spheres are located at [98]

$$\partial_r \frac{f(r)}{h(r)}\bigg|_{r=r_{ph}} = 0. \tag{13}$$

Also, the shadow of the black hole, which indicates the region which no light can escape for the asymptotically flat metric of form Eq. (1) is given by [89,99]

$$r_{sh} = \frac{r_{ph}}{\sqrt{f(r_{ph})}} = \frac{r_{ph}^{3/2}\sqrt[4]{R^2 + r_{ph}^2}}{\sqrt{-2M\sqrt{R^2 + r_{ph}^2} + r_{ph}\left(8\pi\rho_0 R^3 + \sqrt{R^2 + r_{ph}^2}\right) + 8\pi\rho_0 R^3\sqrt{R^2 + r_{ph}^2}\left(\log\left(\sqrt{R^2 + r_{ph}^2} - r_{ph}\right) - \log(R)\right)}}. \tag{14}$$

Figure 3 displays the photon radius and shadow of the black hole versus R_s/M for three cases of $\rho_0 M^2$.

As previously mentioned, in the limit of small R and ρ_0, Eq. (3) converges to the lapse function of the Schwarzschild black hole. This is also evident in Fig. 3. As R and ρ_0 approach zero, the size of the photon sphere and the shadow of the black hole become equal to those of the Schwarzschild black hole. Furthermore, increasing the parameters R and ρ_0 leads to a corresponding increase in the sizes of these radii.

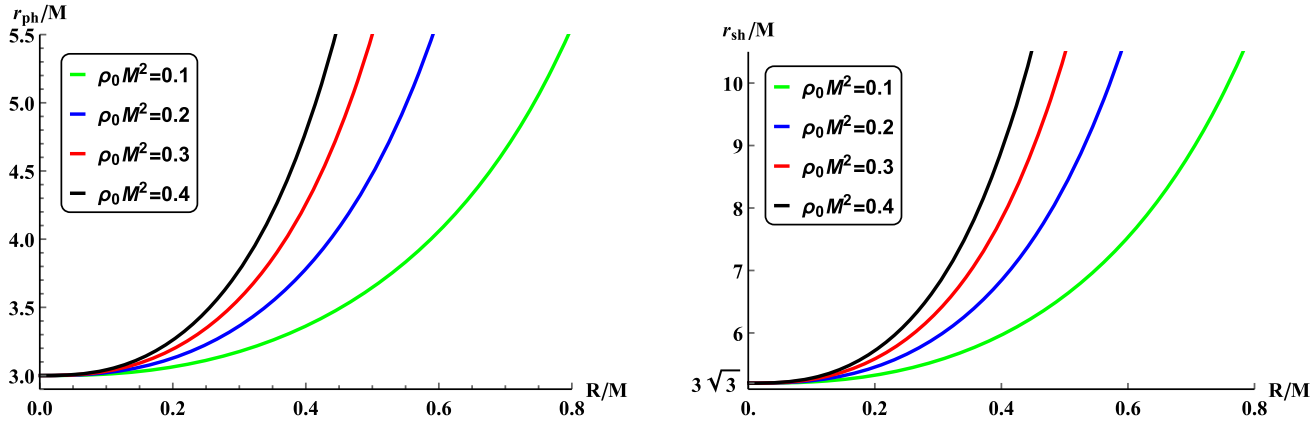

Fig. 3 Left panel: photon radius by varying R/M. Right panel: shadow radius as function of R/M

3.2 Emission rate

The rate of emission energy in black hole physics is a fundamental concept that describes how energy escapes from a black hole through quantum processes. This phenomenon primarily arises from quantum fluctuations in the spacetime surrounding the black hole, leading to the creation and annihilation of virtual particle pairs. When these pairs form near the event horizon, one particle may fall into the black hole while the other escapes, resulting in a net loss of energy from the black hole. This quantity is computed from [100]

$$\frac{d^2E}{d\omega dt} = \frac{2\pi^2\sigma\omega^3}{\exp(\omega/T_{\rm H})-1}, \tag{15}$$

where ω refers to the photon frequency, $T_{\rm H}$ represents Hawking temperature and σ indicates the cross section area in employing Eq. (14) is obtained from $\sigma = \pi r_{sh}^2$ [101]. The variations of energy emission rate as a function of frequency is illustrated in Fig. 4 for different parameter values.

It is observed that the emission rate reaches its maximum with increasing frequency, after which it declines and approaches zero at higher frequencies. The Schwarzschild black hole exhibits a higher energy emission rate compared to the Schwarzschild black hole in the presence of King dark matter. Additionally, increasing the size of the parameters R and ρ_0 results in a decrease in the emission rate shifting its maximum to a lower frequency.

4 The quasi-normal modes analysis of the black hole spacetime

This section explores the dynamics of massless scalar perturbations within the regular black hole spacetime defined by the metric function derived from the King dark matter density profile.

Assuming negligible back-reaction on the background geometry, we treat the spacetime as a fixed arena for perturbation analysis, enabling a focus on the stability and oscillatory behavior of the black hole. The evolution of the massless scalar field is governed by a Schrödinger-like wave equation of the Klein–Gordon type, expressed in the tortoise coordinate r_* (where $\frac{dr_*}{dr} = f(r)$) as

$$\partial^2_{r_*}\psi(r_*)_{sl} + \omega^2\psi(r_*)_{sl} = V_s(r)\psi(r_*)_{sl},$$

with the effective potential [102,103]

$$V_s(r) = f(r)\left(\frac{l(l+1)}{r^2} + \frac{1}{r}\frac{d}{dr}f(r)\right), \tag{16}$$

where l is the multipole moment and ω the complex frequency encoding oscillation and damping of the ring-down gravitational waves. Using numerical results of the QNMs, this investigation tries to reveal how the dark matter parameter $\alpha = 8\pi\rho_0 R^2$ modifies the QNM spectrum due to the polyhomogeneous spacetime structure. The maximum of $V_s(r)$, located where $\frac{\partial}{\partial r}V_s(r)\big|_{r=r_{peak}} = 0$, determines the barrier height influencing QNM stability, offering insights into the black hole's response to scalar perturbations and its potential role in gravitational wave signatures.

We have shown the variation of the scalar potential in Fig. 5. The plots suggest that the dark matter significantly affects the potential structure. An increase in the parameter α, on the right panel of the Fig. 5, results in a decrease of the size of the potential shape and a shift of the peak of the potential towards the right or higher r/R values.

To investigate the QNMs of the black hole spacetime under consideration, we employ two distinct methods: the analytical Mashhoon method [104,105] and the semi-analytical 3rd-order Wentzel–Kramers–Brillouin WKB approximation. These approaches allow us to compute the QNM frequencies associated with scalar field perturbations in a modified gravity background with a mass-to-length scale param-

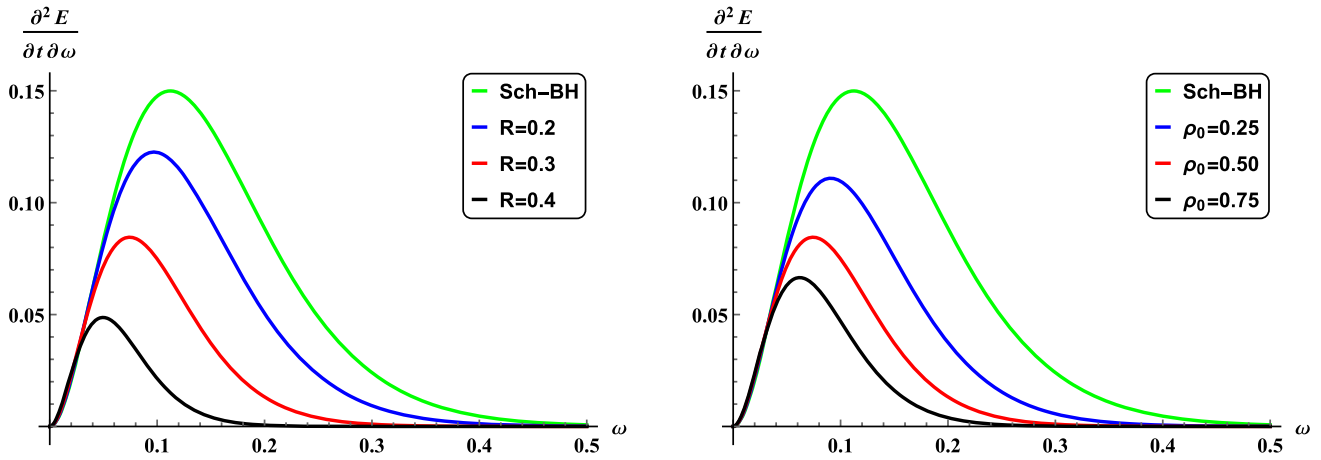

Fig. 4 The behavior of emission rate considering $M = 1$. Left panel: $\rho_0 = 0.5$. Right panel: $R = 0.3$

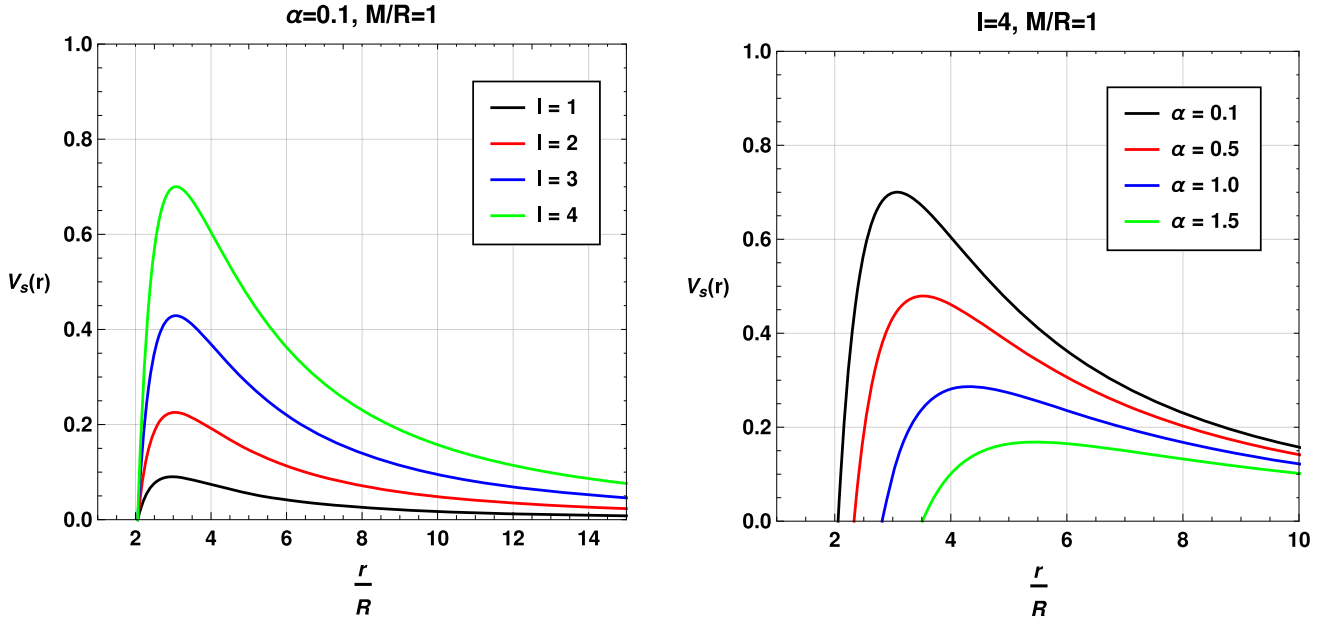

Fig. 5 Variation of potential for scalar perturbation

eter ratio $M/R = 1$. The Mashhoon method provides an elegant analytical estimate, while the WKB method offers higher precision for a broader range of modes. Below, we describe the methodologies and present a comparison of their results.

4.1 Mashhoon method

The Mashhoon method is an analytical technique that approximates the effective potential of perturbations by matching it to a solvable potential, specifically the Pöschl–Teller potential, defined as:

$$V_{\mathrm{PT}}(r_*) = \frac{V_0}{\cosh^2\left[a(r_* - r_{*0})\right]}, \tag{17}$$

where V_0 is the maximum height of the potential, a encodes its curvature at the peak location r_{*0}, and r_* is the tortoise coordinate. This approximation is particularly effective near the potential's maximum, where the effective potential for black hole perturbations often resembles the Pöschl–Teller form due to its smooth, bell-shaped profile.

To apply the Mashhoon method, we first derive the effective potential $V_s(r)$ for scalar perturbations in the black hole spacetime. We identify the peak of $V_s(r)$, evaluate its value (V_0) and second derivative at the peak to determine a, and then compute the QNM frequencies using the analytical expression for the Pöschl–Teller potential:

$$\omega = \omega_R + i\omega_I = \sqrt{V_0 - \frac{a^2}{4}} - ia\left(n + \frac{1}{2}\right), \tag{18}$$

Table 1 QNMs using Mashhoon method with $M/R = 1$

$\alpha(=8\pi\rho_0 R^2)$	l	n	ω
0.3	3	0	$0.758717 - 0.0787689i$
0.3	3	1	$0.758717 - 0.236307i$
0.3	4	0	$0.758717 - 0.0787689i$
0.3	4	1	$0.758717 - 0.236307i$
0.5	3	0	$0.688837 - 0.0688453i$
0.5	3	1	$0.688837 - 0.206536i$
0.5	4	0	$0.688837 - 0.0688453i$
0.5	4	1	$0.688837 - 0.206536i$

where n is the overtone number, and ω_R and ω_I are the real and imaginary parts of the QNM frequency, respectively. This method is particularly efficient for fundamental modes ($n = 0$) and large angular momentum numbers (l), providing qualitative insights into the QNM spectrum with minimal computational cost.

Table 1 presents the QNM frequencies calculated using the Mashhoon method for $\alpha = 0.3$ and $\alpha = 0.5$, with $l = 3, 4$ and $n = 0, 1$. The results show the characteristic behavior of QNMs, where the real part of ω remains constant for a given α and l, while the imaginary part increases in magnitude with the overtone number n.

4.2 Comparison with 3rd-order WKB method

To complement the Mashhoon method, we also compute QNM frequencies using the 3rd-order WKB approximation, which provides higher accuracy for a wider range of modes by incorporating higher-order corrections to the effective potential. The WKB method is particularly suited for numerical computations of QNMs [106–117], capturing subtle variations in the potential that may be oversimplified in the Mashhoon approach.

Table 2 compares the QNM frequencies for $\alpha = 0.1$, $n = 0$, and $l = 1$ to 8, calculated using both the Mashhoon and 3rd-order WKB methods. The table includes the absolute differences in the real and imaginary parts of the frequencies to quantify the agreement between the two methods. The results are rounded to 5 decimal places for clarity.

The results in Table 1 demonstrate that the Mashhoon method yields consistent QNM frequencies for fixed α and l, with the imaginary part of ω scaling linearly with $n + 1/2$, as expected from the Pöschl–Teller approximation. For $\alpha = 0.3$, the real part of the QNM frequency is approximately 0.758717 for $l = 3, 4$, while for $\alpha = 0.5$, it decreases to 0.688837, reflecting the influence of the modified gravity parameter α.

Table 2 reveals that the 3rd-order WKB method and the Mashhoon method produce QNM frequencies that are in close agreement for $\alpha = 0.1$, particularly for higher l. The absolute differences in the real and imaginary parts decrease as l increases, with the smallest differences observed for $l = 8$ (0.00111 for the real part and 0.00089 for the imaginary part). This trend suggests that the Mashhoon method becomes increasingly accurate for larger l, where the effective potential is better approximated by the Pöschl–Teller form. However, for lower l (e.g., $l = 1$), the differences are more significant (0.00701 for the real part and 0.00150 for the imaginary part), indicating that the WKB method captures additional corrections not accounted for in the Mashhoon approximation. Another point to mention here is that the accuracy of the WKB method increases with an increase in the values of $l - n$. As l is close to n, the method provides more error. So, this also may be the discrepancy observed in the QNMs for lower l values.

The Mashhoon method's simplicity makes it a valuable tool for qualitative insights, however, the WKB method provides more accurate results, especially for fundamental modes ($n = 0$) and large l. Together, these methods offer complementary perspectives on the QNM spectrum, confirming the robustness of the calculated frequencies in the modified gravity background.

The plots shown in Figs. 6 and 7 illustrate the variation of QNMs with respect to the model parameter $\alpha = 8\pi\rho_0 R^2$ for scalar perturbations, calculated using the Mashhoon method, for a regular black hole solution derived from the King dark matter density profile. Figure 6 shows the real and absolute of imaginary parts of the QNMs decreasing with increasing α, indicating a decrease in damping of oscillations and a reduction in the oscillation frequency as the density parameter grows, which reflects the influence of the dark matter halo on the black hole's perturbation dynamics. Figure 7 presents a contour plot highlighting the continuous transition of QNMs, suggesting a smooth dependence on α. Physically, this behaviour implies that the regular black hole, characterised by a non-singular metric function $f(r)$, exhibits modified stability properties compared to the Schwarzschild solution, with the dark matter contribution potentially affecting the spacetime against perturbations, especially for $\alpha > 0$. Our investigation implies that in the presence of King's dark matter, the oscillation frequency of ring-down gravitational waves decreases, and along with that, the possibility of detection also increases as the presence of dark matter slows down the decay rate of QNMs.

5 Evolution of perturbations: time domain profiles

In the preceding section, we numerically computed the QNMs and analyzed their behavior with respect to the model parameters using the 3rd-order Wentzel–Kramers–Brillouin (WKB) approximation and the Mashhoon method. In this section, we focus on the time domain evolution of mass-

Table 2 Comparison of QNM frequencies for $\alpha\ (=8\pi\rho_0 R^2) = 0.1$, $n = 0$ and $M/R = 1$.

l	ω_{WKB}	ω_{Mashhoon}	$\lvert\text{Re}(\omega_{\text{WKB}}) - \text{Re}(\omega_{\text{Mashhoon}})\rvert$	$\lvert\text{Im}(\omega_{\text{WKB}}) - \text{Im}(\omega_{\text{Mashhoon}})\rvert$
1	0.27845 − 0.09188i	0.28546 − 0.09338i	0.00701	0.00150
2	0.46225 − 0.09082i	0.46621 − 0.09085i	0.00396	0.00003
3	0.64598 − 0.09057i	0.64875 − 0.09011i	0.00277	0.00046
4	0.82985 − 0.09047i	0.83197 − 0.08980i	0.00212	0.00067
5	1.01380 − 0.09042i	1.01553 − 0.08965i	0.00173	0.00077
6	1.19780 − 0.09039i	1.19926 − 0.08956i	0.00146	0.00083
7	1.38185 − 0.09037i	1.38311 − 0.08950i	0.00126	0.00087
8	1.56591 − 0.09036i	1.56702 − 0.08946i	0.00111	0.00089

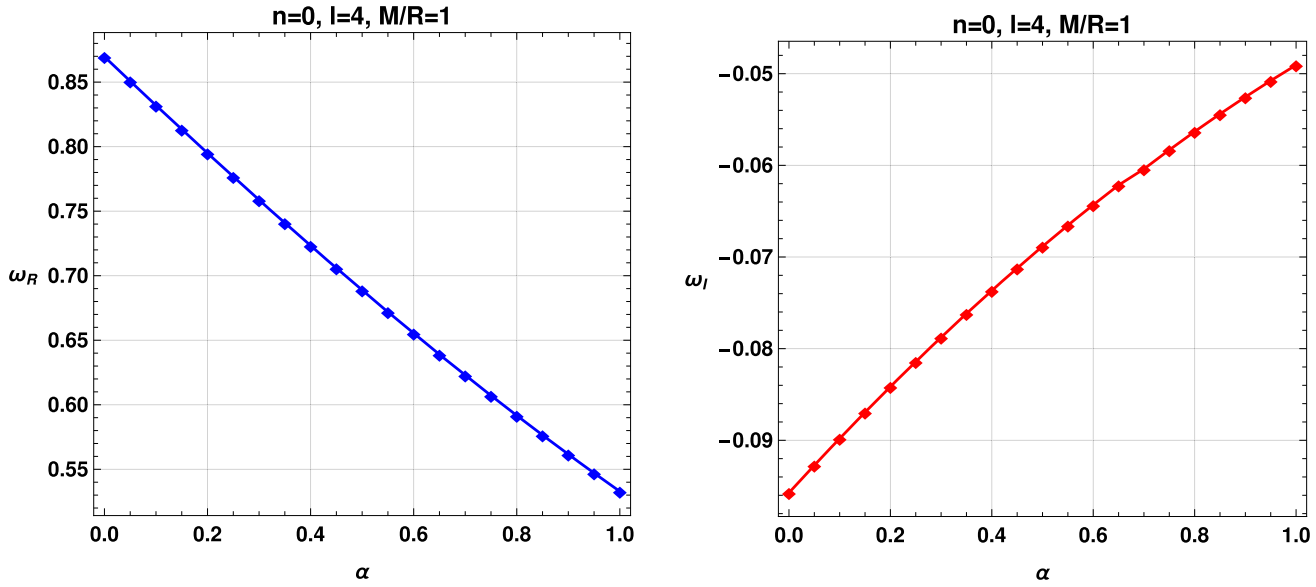

Fig. 6 Variation of QNMs with respect to model parameter $\alpha = 8\pi\rho_0 R^2$ for scalar perturbation

less scalar perturbations, providing a detailed examination of their temporal profiles. The numerical methodology for obtaining time domain profiles was first introduced by Gundlach et al. [118]. Here, we adopt the time domain integration formalism outlined in [119] to compute the evolution of the scalar field.

To model the time evolution, we define the scalar field as $\psi(r_*, t) = \psi(i\Delta r_*, j\Delta t) = \psi_{i,j}$, where r_* is the tortoise coordinate and t is time, with i and j indexing the spatial and temporal grids, respectively. The effective potential is denoted as $V(r(r_*)) = V(r_*, t) = V_{i,j}$. The wave equation governing the scalar perturbation is discretized as

$$\frac{\psi_{i+1,j} - 2\psi_{i,j} + \psi_{i-1,j}}{\Delta r_*^2} - \frac{\psi_{i,j+1} - 2\psi_{i,j} + \psi_{i,j-1}}{\Delta t^2} - V_i\psi_{i,j} = 0. \tag{19}$$

We impose the initial condition $\psi(r_*, t) = \exp\left[-\frac{(r_*-k_1)^2}{2\sigma^2}\right]$ at $t = 0$, representing a Gaussian wave packet with median

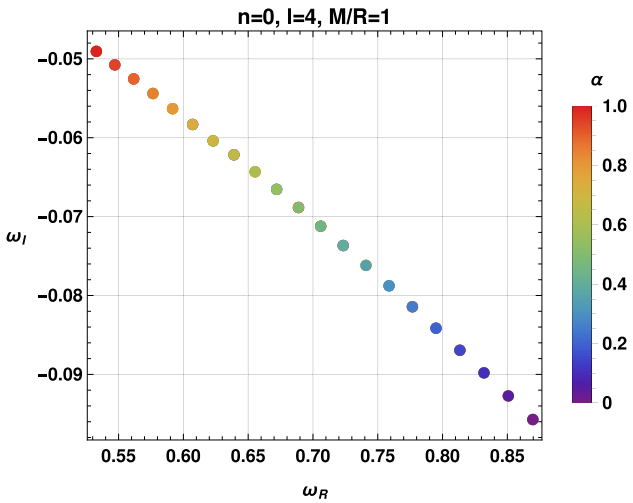

Fig. 7 Contour with variation of model parameter $\alpha = 8\pi\rho_0 R^2$ for scalar perturbation

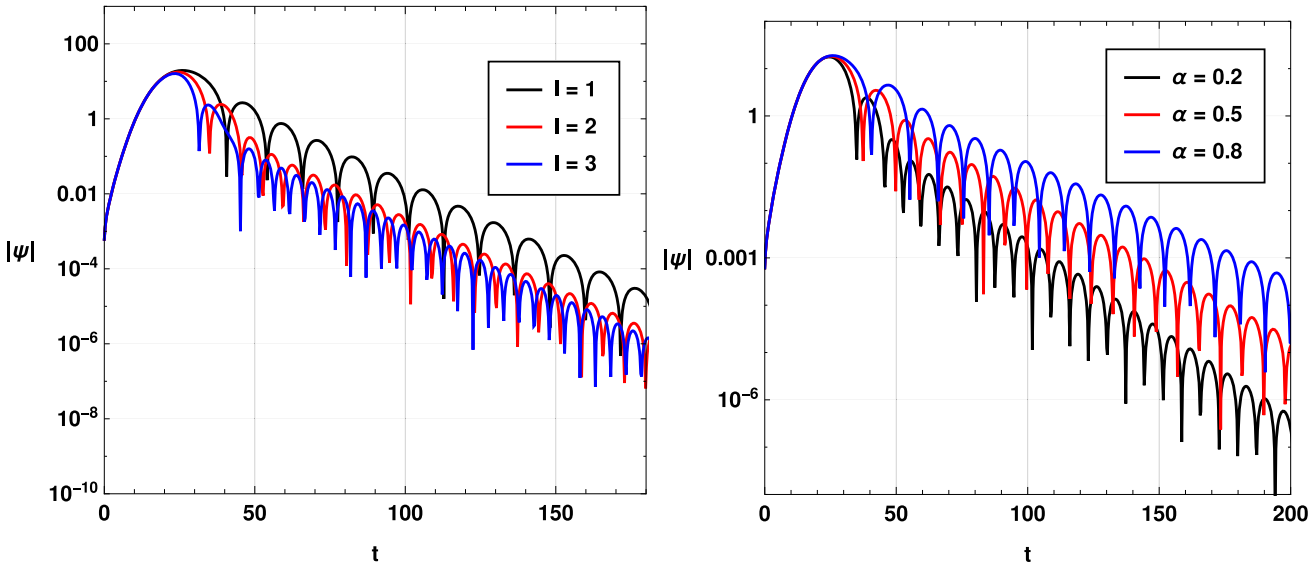

Fig. 8 Time domain profiles for fundamental scalar perturbations with $M/R = 1$. The left panel shows the evolution for multipole numbers $l = 1, 2, 3$ with fixed $\alpha = 0.2$. The right panel shows the evolution for varying α with fixed $l = 2$

k_1 and width σ, and set $\psi(r_*, t) = 0$ for $t < 0$. The time evolution of the scalar field is computed using the iterative scheme

$$\psi_{i,j+1} = -\psi_{i,j-1} + \left(\frac{\Delta t}{\Delta r_*}\right)^2 (\psi_{i+1,j} + \psi_{i-1,j}) + \left(2 - 2\left(\frac{\Delta t}{\Delta r_*}\right)^2 - V_i \Delta t^2\right) \psi_{i,j}. \tag{20}$$

To ensure numerical stability, we maintain the ratio $\frac{\Delta t}{\Delta r_*} < 1$, satisfying the Von Neumann stability condition. This scheme allows us to compute the temporal profile of $\psi(r_*, t)$ for a fixed grid resolution.

The time domain profiles of the massless scalar perturbations are illustrated in Fig. 8. The first panel depicts the evolution of the scalar field for different values of the multipole number $l = 1, 2, 3$, with a fixed model parameter $\alpha = 0.2$ and mass-to-radius ratio $M/R = 1$. The second panel illustrates the effect of varying the model parameter α, with a fixed multipole number $l = 2$. In the first panel, for a fixed $\alpha = 0.2$, the scalar field's amplitude increases over time, with the rate of increase varying significantly with l. Lower values of l (e.g., $l = 1$) exhibit a slower rise in amplitude compared to higher values (e.g., $l = 3$), indicating that higher multipole moments lead to faster growth in the perturbation amplitude. This behavior is consistent with the physical expectation that higher angular momentum modes, associated with larger l, couple more strongly to the background geometry, resulting in more rapid dynamical evolution.

In the second panel, for a fixed $l = 2$, varying α alters the temporal evolution of the scalar field. Smaller values of α result in a steeper increase in the amplitude, suggesting that the model parameter α modulates the strength of the interaction between the scalar field and the effective potential. As α increases, the growth rate diminishes, indicating a stabilizing effect on the perturbation dynamics. This suggests that α plays a critical role in regulating the energy transfer within the system, potentially affecting the decay or amplification of perturbations.

6 Greybody bounds, emitted power, and partial absorption cross section

Greybody bounds refer to the frequency-dependent factors that characterize the radiation emitted by black holes in the context of Hawking radiation [120–122]. This factor accounts for the influence of potential barriers surrounding the black hole, which filter the emitted radiation and using Eq. (3) is computed from [123,124]

$$T_l(\omega) \geq \text{sech}^2\left(\frac{1}{2\omega}\int_{r_h}^{\infty} V_{\text{eff}}(r)\frac{dr}{f(r)}\right), \tag{21}$$

where ω indicates the frequency, l represents the multipole quantum number, and $V_{\text{eff}}(r)$ is an effective potential that influence the escape of radiation and is presented in Eq. (16) Figure 9 illustrates the curve of greybody bounds for the mode $l = 1$ and various selections of other parameters.

It is evident that, unlike the full radiation of a black body, which is independent of frequency, greybody bounds is dependent on frequency variations. Additionally, it is observed that for the Schwarzschild black hole, the value of greybody bound at a fixed frequency is lower compared to that of a black hole in the presence of King dark matter. Furthermore, increasing the parameter $R\,(\rho_0)$ while keep-

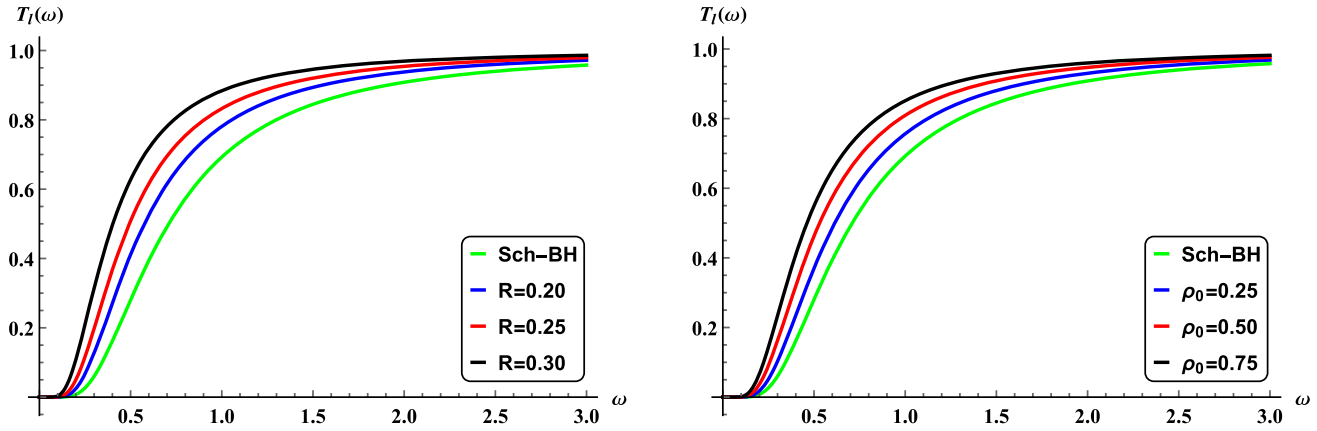

Fig. 9 Greybody bounds as function of frequency considering $M = 1$ and $l = 1$ for left panel: $R = 0.3$, and right panel: $\rho_0 = 1$

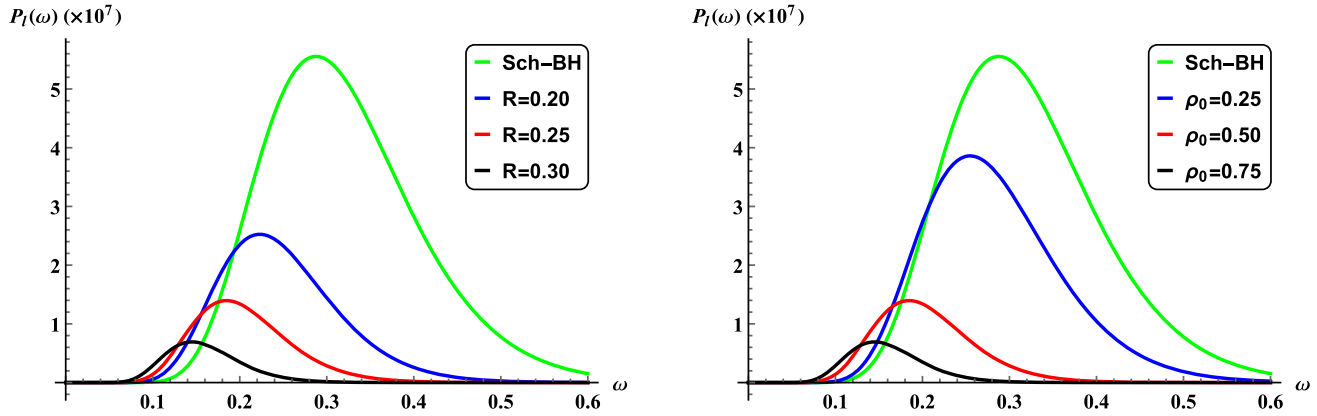

Fig. 10 Variations in emitted power in terms of ω considering $M = 1$ and $l = 1$ for left panel: $\rho_0 = 1$ and right panel: $R = 0.3$

ing other parameters constant results in a larger value of greybody bound. At high frequencies, the greybody factor approaches unity, allowing energetic particles to pass through the black hole's potential barrier easily. In this case, most incoming particles can enter the black hole. However, at lower frequencies, the barrier becomes more significant. Our findings show that increasing the scale radius R raises the chances of particle transmission, suggesting that dark matter alters the potential in a way that helps particles pass through. Higher density parameters ρ_0 also reduce the barrier's impact, making it easier for particles to propagate.

Another quantity related to the greybody bound is the emitted power by black hole and is defined as [91,125,126]

$$P_l(\omega) = \frac{A}{8\pi^2} T_l(\omega) \frac{\omega^3}{\exp(\omega/T_{\rm H}) - 1}, \tag{22}$$

that A represents to the horizon surface and $T_{\rm H}$ refers to the Hawking temperature. Figure 10 displays the emitted power curve for various parameter selections as a function of frequency.

The emitted power increases with rising frequency, reaching a maximum and then gradually decreasing toward zero. The maximum value of this quantity for the Schwarzschild black hole is greater than that for a black hole in the presence of King dark matter. As R or ρ_0 increases, the peak of the emission spectrum shifts to lower frequencies, resulting in a redder spectrum. The peak height also decreases, meaning a black hole surrounded by dark matter radiates less efficiently than an isolated one. The dark matter halo lowers the Hawking temperature, causing the black hole to emit like a cooler body with less power, further shifting the emission peak to lower frequencies.

The partial absorption cross section of a black hole measures its ability to capture various types of incoming radiation, such as scalar, electromagnetic, and gravitational waves and is defined as the effective area that quantifies the probability of a specific mode of radiation being absorbed by a black hole and considering Eq. (21) is given by [127,128]

$$\sigma^l_{abs}(\omega) = \frac{\pi(2l+1)}{\omega^2} |T_l(\omega)|^2. \tag{23}$$

Figure 11 shows the behavior of absorption cross section for various parameter selections as a function of frequency.

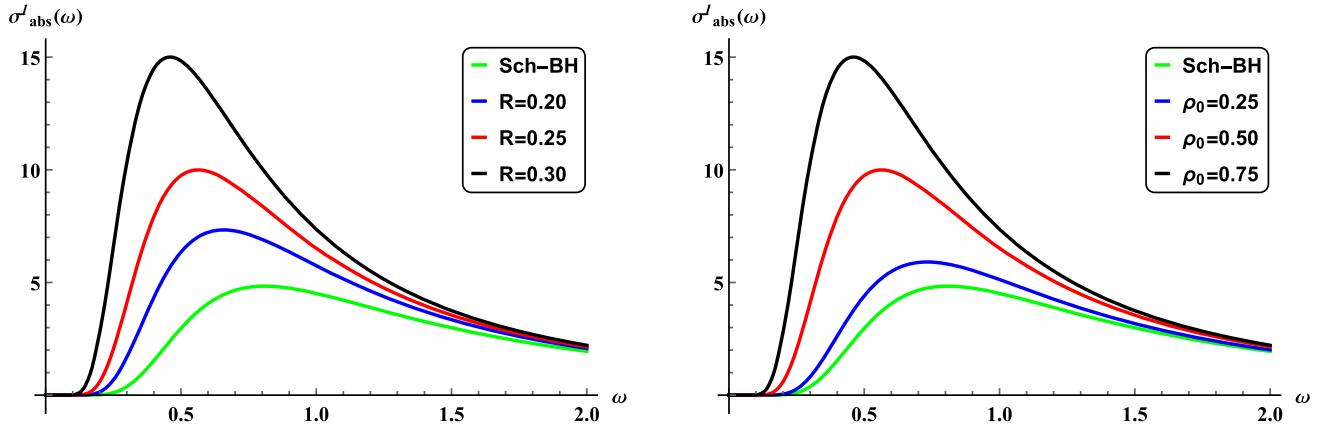

Fig. 11 The behavior of partial absorption cross section is terms of frequency where $M = 1$ and $l = 1$ for left panel $\rho_0 = 1$ and for right panel $R = 0.3$

At low frequencies, the wavelength of the radiation is larger than the black hole itself, causing it to behave as a point-like object. In this regime, only the spherically symmetric monopole mode plays a significant role, leading to a cross section that approximates the area of the black hole's horizon. It is clear that increasing frequency leads to an increase in absorption, which reaches its maximum value and then at high frequencies, where the wavelength is much smaller than the horizon, radiation acts more like classical particles and gradually decreases. Here, the absorption characteristics are governed by the dynamics near the photon sphere, resulting in oscillations around a geometrical optics limit. When King dark matter is present, these dynamics change. At low frequencies, the halo increases the effective horizon radius, which enlarges the absorption cross section compared to an isolated Schwarzschild black hole. This increase is more pronounced with greater halo density or scale radius. At high frequencies, the halo alters the position of the photon sphere, which in turn reduces the efficiency of capturing high-frequency radiation and shifts the oscillatory peaks to lower frequencies. Thus, dark matter significantly influences the absorption properties of black holes across different frequency ranges. It is observed that, for the Schwarzschild black hole at a fixed frequency, the absorption value is lower compared to that of a black hole in the presence of King dark matter. Moreover, increasing R (ρ_0) not only increases the absorption value but also results in the maximum occurring at a lower frequency.

7 The periodic motion of a particle around the black hole in King dark matter halo

The Lagrangian of a timelike test particle moving freely around the black hole in King dark matter halo can be written as

$$2\mathcal{L} = -f(r)\dot{t}^2 + f^{-1}(r)\dot{r}^2 + h(r)\dot{\varphi}^2 = -1, \tag{24}$$

where assuming its motions are confined in the equatorial plane $\theta = \pi/2$ and the dot in this expression indicates the differentiation with respect to the proper time. Then, the motions of particle have two constants which are related to the energy and angular momentum of the particle, respectively, and can be expressed as

$$E = f(r)\dot{t}, \tag{25}$$

$$L = h(r)\dot{\varphi}. \tag{26}$$

Based on this two constants, the equation of radial motion of particles can be written as

$$\dot{r}^2 = E^2 - V_{\text{eff}}, \tag{27}$$

where V_{eff} is the effective potential and can be defined as

$$V_{\text{eff}} = f(r)\left[1 + \frac{L^2}{h(r)}\right]. \tag{28}$$

For a given energy E and angular momentum L, the bound orbit of a timelike test particle moving around the black hole in King dark matter halo can be described by a simple, number p as [49]

$$p = \frac{\Delta\varphi}{2\pi} - 1, \tag{29}$$

with the accumulated azimuth $\Delta\varphi$ between successive periastrons during a radial period calculated as

$$\Delta\varphi = 2\int_{r_-}^{r_+} \frac{\mathrm{d}\varphi}{\mathrm{d}r}\mathrm{d}r = 2\int_{r_-}^{r_+} \frac{L}{h(r)}\sqrt{\frac{1}{E^2 - V_{\text{eff}}}}\mathrm{d}r, \tag{30}$$

where Eqs. (26) and (27) are be used and $r_\pm$ are two turning points of the bound orbit, i.e., the roots of $\dot{r}^2 = 0$. We can

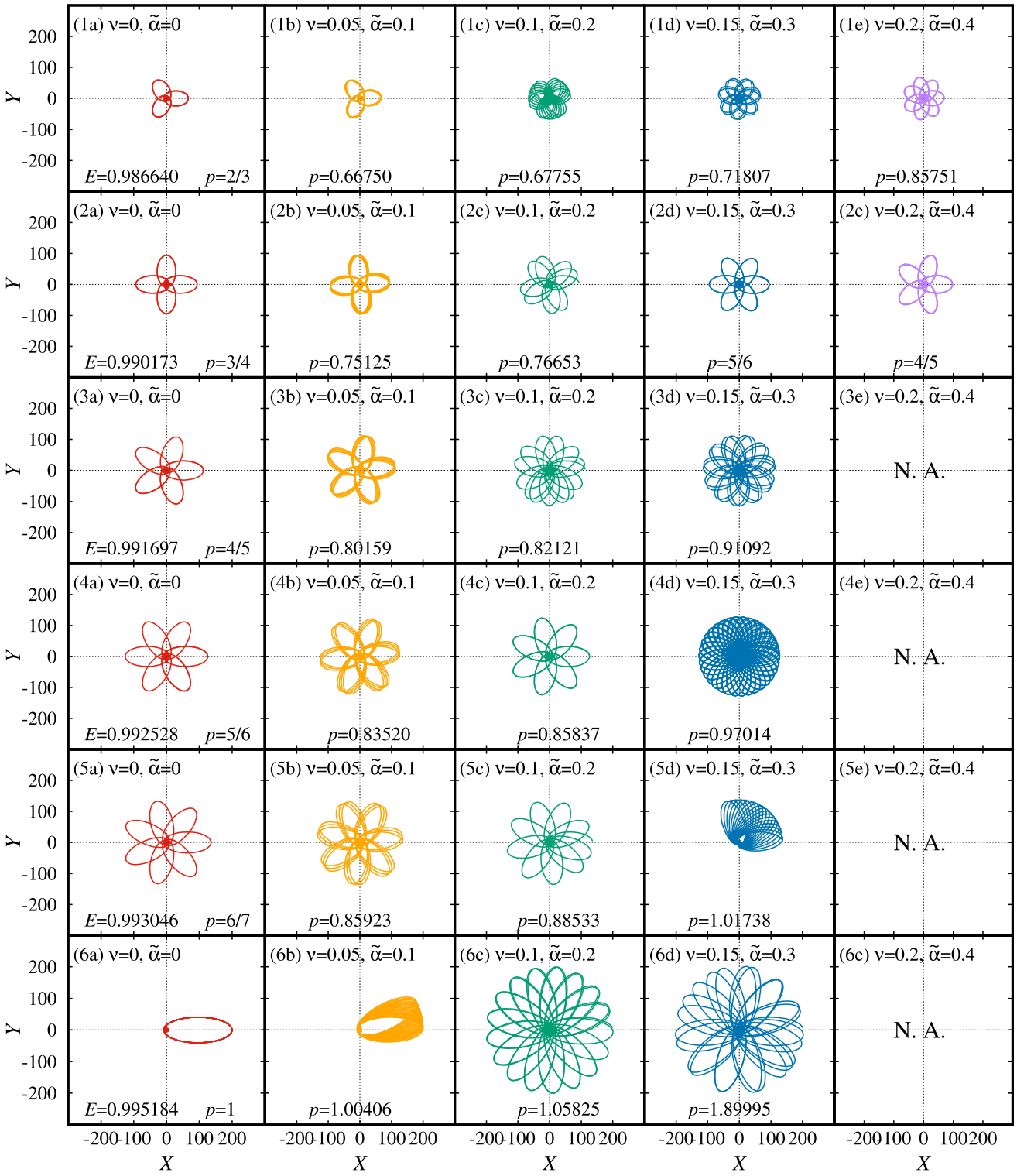

Fig. 12 Some examples of bound orbits around the black hole in King dark matter halo with angular momentum $l = L/M = 3.98$, where $(X, Y) = (x\cos\varphi, x\sin\varphi)$, $x = r/M$ and the unique p is denoted in each panel. Each row shares the same energy E. The particular periodic orbits are set in the first column with the dimensionless central density $\nu = \rho_0 M^2 = 0$ and the length scale parameter $\tilde{\alpha} = R/M = 0$. The notation of "N. A." means that no bound orbit exists in the panel with particular energy E, angular momentum l, dimensionless central density ν and length scale parameter $\tilde{\alpha}$

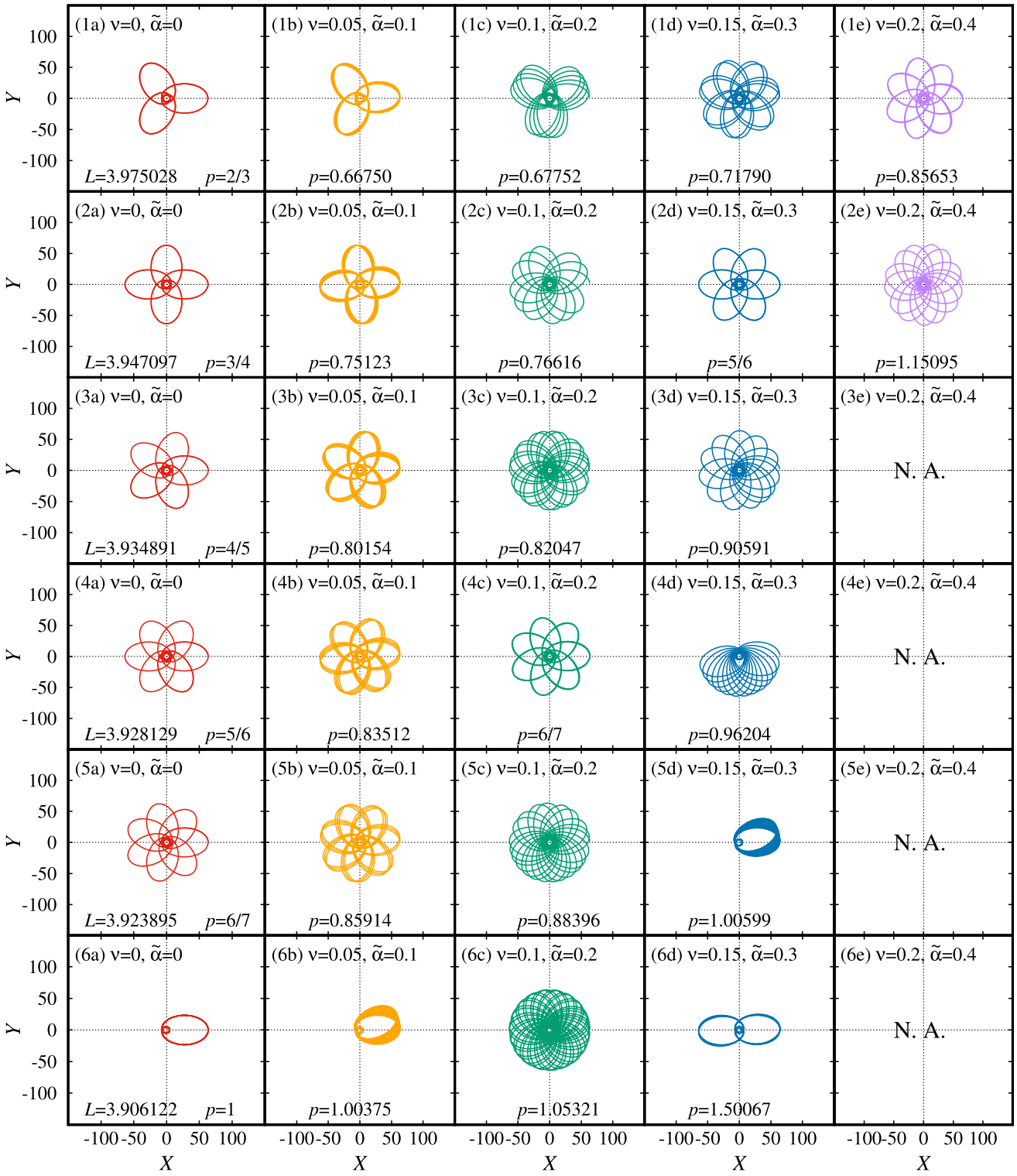

Fig. 13 Some examples of bound orbits around the black hole in King dark matter halo with energy $E = 0.986$, where $(X, Y) = (x\cos\varphi, x\sin\varphi)$, $x = r/M$ and the unique p is denoted in each panel. Each row shares the same angular momentum $l = L/M$. The particular periodic orbits are set in the first column with the dimensionless central density $\nu = \rho_0 M^2 = 0$ and the length scale parameter $\tilde{\alpha} = R/M = 0$. The notation of "N. A." means that no bound orbit exists in the panel with particular energy E, angular momentum l, dimensionless central density ν and length scale parameter $\tilde{\alpha}$

see that Eq. (29) indicate for a rational value of p, the test particle returns to its starting point after a finite period, forming a periodic orbit. Conversely, an irrational p results in a precessing orbit around the black hole in King dark matter halo.

Unlike the near-elliptical trajectories of precessing orbits, these periodic orbits exhibit a diverse range of patterns. This diversity necessitates expressing the rational number p as a set of three integers (z, w, v) as [49]

$$p = w + \frac{v}{z}, \tag{31}$$

where z is the zoom number, denoting the number of leaves in the orbit; w is the whirl number, representing the number of near-circular revolutions around the periastron per leaf; v is the vertex number, indicating the sequence in which the z leaves are formed.

To illustrate the characteristics of periodic motions of particles around a black hole in King dark matter halo, we have plotted multiple bound orbits with a fixed angular momentum $l = L/M = 3.98$ but varying energies E near this celestial object, as shown in Fig. 12, where $(X, Y) = (x\cos\varphi, x\sin\varphi)$ and $x = r/M$. Each row of the figure corresponds to a fixed energy value E, and the dimensionless central density ν and the dimensionless length scale parameter $\tilde{\alpha}$ of each panel increases from left to right, denoting as $\nu = \rho_0 M^2$ and $\tilde{\alpha} = R/M$, respectively. The first column shows periodic orbits with a specific value of p under the condition $\nu = 0$ and $\tilde{\alpha} = 0$, which corresponds to the classical Schwarzschild black hole. The remaining columns display particle trajectories near the black hole in King dark matter halo, with the respective value of p indicated in each panel. As can be seen from the figure, the value of p in each row increases with the growth of both the dimensionless central density ν and the length scale parameter $\tilde{\alpha}$. This indicates that the presence of dark matter halo leads to a larger value of p for particle motion around the black hole compared to the Schwarzschild case. For particles with higher energy, an increase in the dimensionless central density ν and the length scale parameter $\tilde{\alpha}$ can cause their orbits to transition from bound to unbound one, such as (6a) to (6e) in Fig. 12, which could be one of the key features that distinguish this black hole from the classical Schwarzschild black hole. Furthermore, the presence of dark matter halo also causes the periodic orbits of particles around this black hole to exhibit the same characteristics as those around a Schwarzschild black hole. For instance, both the subfigures (2e) and (3a) in Fig. 12 present a periodic orbit with $p = 5/6$ but with a different energy.

Figure 13 also depicts bound orbits around the black hole in King dark matter halo for a fixed energy of $E = 0.986$. Each row corresponds to a specific value of the rescaled angular momentum l, and the overall layout is similar to that of Fig. 12. Similarly, the figure shows that for a given angular momentum, the value of p for particle bound orbits increases with the dimensionless central density ν and the length scale parameter $\tilde{\alpha}$. When the angular momentum l of the particle is sufficiently small, the presence of the dark matter halo may cause its orbit to transition from bound to unbound, such as the (5a) to (5e) of the Fig. 13. Furthermore, under such conditions, variations in the dimensionless central density ν and length scale parameters $\tilde{\alpha}$ can also lead to particles with different angular momenta l forming identical periodic orbits, as shown by (2d) → (4a) and (4c) → (5a) of the Fig. 13. Fig. 14 shows the range of energy and angular momentum values for which particles can form bound orbits around a black hole embedded in a King dark matter halo.

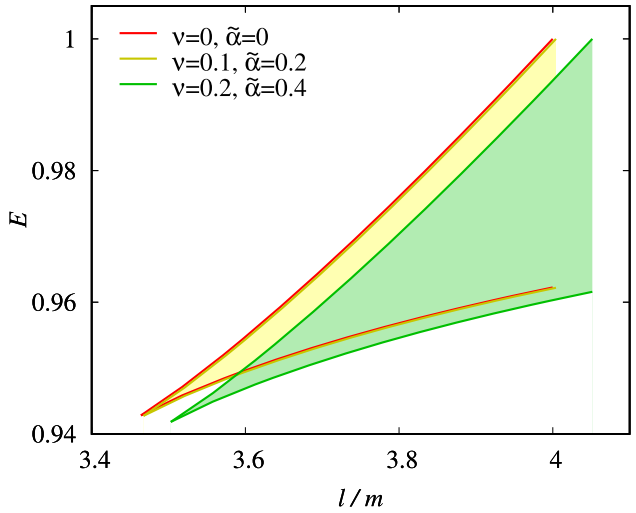

Fig. 14 The range of energy and angular momentum required for particles to form bound orbits around the black hole in King dark matter halo is shown by the shaded area in the figure

8 Conclusion

In this study, we investigated the Schwarzschild black hole surrounded by King dark matter. We analyzed the sparsity of Hawking radiation and observed that an increase in the parameters of dark matter leads to heightened sparsity. However, this effect diminishes at larger values of r_h.

We explored the impact of King dark matter on the emission rate, finding that as the influence of the dark matter parameters increases, the emission rate decreases at constant frequencies, while the maximum emission rate shifts to lower frequencies.

In addition to the thermodynamic and emission analyses, a detailed examination of the QNMs was conducted to investigate the dynamical stability of the Schwarzschild black hole surrounded by King dark matter. The QNM spectra, obtained

using both the analytical Mashhoon method and the semi – analytical 3rd – order WKB approximation, exhibit remarkable consistency, especially for higher multipole numbers. The comparison between the two approaches demonstrates that the differences in the real and imaginary parts of the frequencies diminish with increasing l, confirming the robustness of the results. The analysis revealed that the real part of the QNM frequencies decreases with increasing dark matter parameter α, indicating a suppression in the oscillation frequency of the scalar perturbations. Concurrently, the magnitude of the imaginary part also decreases, signifying a slower decay rate of the ring-down phase. Physically, this behavior suggests that the presence of King dark matter enhances the effective stability of the black hole spacetime, making perturbations more persistent over time.

Furthermore, the variation of the effective potential $V_s(r)$ illustrates that the inclusion of the dark matter parameter α leads to a reduction in the potential barrier height and a shift of its peak toward larger r/R. This structural change in the potential profile directly influences the QNM spectrum, lowering both the oscillation and damping frequencies. Such an effect implies that dark matter modifies the gravitational wave signatures of black holes by altering the frequency and damping characteristics of their ring-down modes. The contour plots of QNM evolution reinforce this interpretation by showing a smooth and continuous dependence of the frequencies on α, suggesting that the transition from vacuum to dark-matter-dominated configurations occurs without any abrupt dynamical instabilities. These findings highlight a crucial role of the surrounding dark matter in modulating black hole perturbations, potentially leading to observable imprints in future gravitational wave observations.

Complementing the frequency-domain analysis, the time-domain evolution of massless scalar perturbations was examined to provide a comprehensive understanding of the black hole's dynamical response. The time-domain profiles reveal that, for a fixed dark matter parameter, higher multipole moments (l) correspond to faster oscillations and more rapid decay of the perturbation amplitude. Conversely, increasing the dark matter parameter α leads to a reduction in the damping rate and amplitude of perturbations, underscoring its stabilizing influence on the system. This behavior is consistent with the QNM results, wherein larger α values correspond to smaller damping rates and lower oscillation frequencies. Together, these results confirm that the presence of King dark matter induces a suppression of scalar perturbations and enhances the longevity of ring-down oscillations, thus contributing to a more stable dynamical configuration.

In essence, the combined frequency and time – domain analyses indicate that King dark matter not only alters the thermodynamic and emission characteristics of the black hole but also leaves a distinct signature on its dynamical stability and gravitational wave spectrum. The reduced damping rate and frequency shift in QNMs point toward a possible observational window into the influence of dark matter on compact objects, particularly in the late-time ring-down phase of gravitational wave signals. These findings provide a foundation for future studies aimed at constraining dark matter profiles through black hole spectroscopy and open new avenues for probing the interplay between astrophysical dark matter environments and black hole dynamics.

Subsequently, we examined the grey body factor of the Schwarzschild black hole in the presence of King dark matter. Our findings indicate that although, at high frequencies, the grey body factor approaches that of black body radiation, at lower frequencies, the enhanced effect of King dark matter parameters results in an increased grey body factor. Furthermore, we observed the emitted power, which decreases with greater influence from the dark matter parameters, with its maximum occurring at lower frequencies. Additionally, the partial absorption cross section increases as the effect of the dark matter parameters intensifies, with its peak shifting to lower frequencies. The investigation of periodic particle motion around the black hole immersed in the King dark matter halo further elucidates the dynamical influence of the surrounding dark matter distribution. The analysis of the effective potential and the resulting orbital structures demonstrates that the presence of dark matter significantly alters the morphology and stability of bound trajectories. Both the dimensionless central density $\nu = \rho_0 M^2$ and the scale parameter $\tilde{\alpha} = R/M$ increase the characteristic parameter $p = \Delta\varphi/2\pi - 1$, leading to enhanced orbital precession compared to the Schwarzschild case. For higher particle energies or lower angular momenta, the dark matter halo can induce transitions from bound to unbound motion, highlighting its impact on the effective gravitational confinement. Moreover, distinct combinations of ν and $\tilde{\alpha}$ may produce identical periodic configurations for different angular momenta, implying a form of orbital degeneracy not present in the classic Schwarzschild spacetime. These results indicate that the King dark matter halo not only modulates the frequency and precession rate of bound orbits but also introduces new dynamical signatures that could, in principle, be reflected in the quasi-periodic oscillations and accretion disk structures around galactic black holes.

Acknowledgements The authors would like to thank the kind referee for their constructive comments. Also, H.H. and S. Z. are grateful to Excellence project FoS UHK 2203/2025-2026 for the financial support. Additionally, D.J.G. acknowledges the contribution of the COST Action CA21136—"Addressing observational tensions in cosmology with systematics and fundamental physics (CosmoVerse)".

Data Availability Statement This manuscript has no associated data. [Author's' comment: Data sharing not applicable to this article as no datasets were generated or analysed during the current study.]

Code Availability Statement This manuscript has no associated code/software. [Author's comment: Code/Software sharing not applicable to this article as no code/software was generated or analysed during the current study.]

Funded by SCOAP[3].

References

1. M. Volonteri, J. Bellovary, Black holes in the early universe. Rep. Prog. Phys. **75**(12), 124901 (2012)
2. G. Landsberg, Black holes at future colliders and beyond. J. Phys. G: Nucl. Part. Phys. **32**(9), R337 (2006)
3. T.M. Heckman, P.N. Best, The coevolution of galaxies and supermassive black holes: insights from surveys of the contemporary universe. Annu. Rev. Astron. Astrophys. **52**(1), 589–660 (2014)
4. B. Carr, F. Kühnel, Primordial black holes as dark matter: recent developments. Annu. Rev. Nucl. Part. Sci. **70**(1), 355–394 (2020)
5. F. Zwicky, Die rotverschiebung von extragalaktischen nebeln. Helvetica Phys. Acta **6**, 110–127 (1933)
6. G. Bertone, D. Hooper, History of dark matter. Rev. Mod. Phys. **90**(4), 045002 (2018)
7. V.C. Rubin, W.K. Ford Jr., Rotation of the andromeda nebula from a spectroscopic survey of emission regions. Astrophys. J. **159**, 379 (1970)
8. V.C. Rubin, W.K. Ford Jr., N. Thonnard, Extended rotation curves of high-luminosity spiral galaxies. IV-Systematic dynamical properties, sa through sc. Astrophys. J. **225**, L107–L111 (1978). (**Part 2-Letters to the Editor**)
9. J.G. de Swart, G. Bertone, J. van Dongen, How dark matter came to matter. Nat. Astron. **1**(3), 0059 (2017)
10. D.N. Spergel, The dark side of cosmology: dark matter and dark energy. Science **347**(6226), 1100–1102 (2015)
11. R.H. Sanders, *The Dark Matter Problem: A Historical Perspective* (Cambridge University Press, Cambridge, 2010)
12. V. Trimble, Existence and nature of dark matter in the universe. Annu. Rev. Astron. Astrophys. **25**(1), 425–472 (1987)
13. L.E. Strigari, Galactic searches for dark matter. Phys. Rep. **531**(1), 1–88 (2013)
14. G. Bertone, T.M.P. Tait, A new era in the search for dark matter. Nature **562**(7725), 51–56 (2018)
15. P. Davies, J. Gribbin, *The Matter Myth: Dramatic Discoveries that Challenge our Understanding of Physical Reality* (Simon and Schuster, New York, 2007)
16. C.V. Vishveshwara, Stability of the Schwarzschild metric. Phys. Rev. D **1**, 2870–2879 (1970)
17. W.H. Press, Long wave trains of gravitational waves from a vibrating black hole. Astrophys. J. Lett. **170**, L105–L108 (1971)
18. S. Chandrasekhar, S. Detweiler, The quasi-normal modes of the Schwarzschild black hole. Proc. R. Soc. Lond. A **344**, 441–452 (1975)
19. C. Ma, Y. Gui, W. Wang, F. Wang, Massive scalar field quasinormal modes of a Schwarzschild black hole surrounded by quintessence. Cen. Eur. J. Phys. **6**, 194–198 (2008)
20. D. Pedrotti, S. Vagnozzi, Quasinormal modes-shadow correspondence for rotating regular black holes. Phys. Rev. D **110**(8), 084075 (2024)
21. R. Oliveira, D.M. Dantas, C.A.S. Almeida, Quasinormal frequencies for a black hole in a bumblebee gravity. EPL **135**(1), 10003 (2021)
22. J.M. Graca, I.P. Lobo, Scalar QNMs for higher dimensional black holes surrounded by quintessence in Rastall gravity. Eur. Phys. J. C **78**(2), 101 (2018)
23. Y. Zhang, Y.X. Gui, F. Li, Quasinormal modes of a Schwarzschild black hole surrounded by quintessence: electromagnetic perturbations. Gen. Relativ. Gravit. **39**, 1003–1010 (2007)
24. M. Bouhmadi-López, S. Brahma, C.-Y. Chen, P. Chen, D. Yeom, A consistent model of non-singular Schwarzschild black hole in loop quantum gravity and its quasinormal modes. JCAP **07**, 066 (2020)
25. D.J. Gogoi, R. Karmakar, U.D. Goswami, Quasinormal modes of nonlinearly charged black holes surrounded by a cloud of strings in Rastall gravity. Int. J. Geom. Methods Mod. Phys. **20**(01), 2350007 (2023)
26. Yassine Sekhmani and Dhruba Jyoti Gogoi, Electromagnetic quasinormal modes of dyonic AdS black holes with quasitopological electromagnetism in a Horndeski gravity theory mimicking EGB gravity at $D \to 4$. Int. J. Geom. Methods Mod. Phys. **20**(09), 2350160 (2023)
27. G. Antoniou, L. Gualtieri, P. Pani, Gravitational quasinormal modes of black holes in quadratic gravity. Phys. Rev. D **111**(6), 064059 (2025)
28. S. Chakraborty, G. Compère, L. Machet, Tidal Love numbers and quasinormal modes of the Schwarzschild–Hernquist black hole. Phys. Rev. D **112**(2), 024015 (2025)
29. M.M. Gohain, K. Bhuyan, H.P. Saikia, Frolov Black Hole Surrounded by Quintessence-II: Quasinormal Modes, Greybody Factors, Deflection Angle and Chaos Bound. 12 (2024)
30. J.. Besson, J.L. Jaramillo, Quasi-normal mode expansions of black hole perturbations: a hyperboloidal Keldysh's approach. Gen. Relativ. Gravit. **57**(7), 110 (2025)
31. Y. Sekhmani, D.J. Gogoi, S.K. Maurya, K. Boshkayev, M.K. Jasim, Quasinormal modes and greybody bounds of black holes endowed with modified Chaplygin gas. JHEAp **45**, 200–213 (2025)
32. A. Kumar, D.V. Singh, S. Upadhyay, Ayón-Beato–García black hole coupled with a cloud of strings: thermodynamics, shadows and quasinormal modes. Int. J. Mod. Phys. A **39**(31), 2450136 (2024)
33. L. Balart, G. Panotopoulos, Á. Rincón, On new regular charged black hole solutions: limiting curvature condition, quasinormal modes and shadows. Ann. Phys. **473**, 169865 (2025)
34. M.O.E. Hadj, Gravitational waves in massive gravity: waveforms generated by a particle plunging into a black hole and the excitation of quasinormal modes and quasibound states. Phys. Rev. D **111**(4), 044055 (2025)
35. A. Kehagias, A. Riotto, Nonlinear effects in black hole ringdown made simple: quasinormal modes as adiabatic modes. Phys. Rev. D **111**(4), L041506 (2025)
36. H. Han, B. Gwak, Quasinormal modes of Plebański–Demiański black hole in the near-Nariai regime. Phys. Rev. D **112**(2), 024031 (2025)
37. D.J. Gogoi, J. Bora, F. Studnička, H. Hassanabadi, Optical, dynamic and topological characteristics of deformed Schwarzschild black holes. JCAP **08**, 009 (2025)

38. M. Skvortsova, Quantum corrected black holes: testing the correspondence between grey-body factors and quasinormal modes. Eur. Phys. J. C **85**(8), 854 (2025)
39. S.-H. Dong, F. Hosseinifar, F. Studnička, H. Hassanabadi, Some new properties of black holes in the quantum Oppenheimer–Snyder model. Phys. Lett. B **860**, 139182 (2025)
40. D.J. Gogoi, U.D. Goswami, Quasinormal modes and Hawking radiation sparsity of GUP corrected black holes in bumblebee gravity with topological defects. JCAP **06**(06), 029 (2022)
41. Z. Dong, D. Zhang, F. Guoyang, W. Jian-Pin, Quasinormal modes of a d-dimensional regular black hole featuring an integrable singularity. Eur. Phys. J. C **85**(2), 215 (2025)
42. L. Pezzella, K. Destounis, A. Maselli, V. Cardoso, Quasinormal modes of black holes embedded in halos of matter. Phys. Rev. D **111**(6), 064026 (2025)
43. D. Laghi, N. Tamanini, W. Del Pozzo, A. Sesana, J. Gair, S. Babak, D. Izquierdo-Villalba, Gravitational-wave cosmology with extreme mass-ratio inspirals. Mon. Not. R. Astron. Soc. **508**(3), 4512–4531 (2021)
44. V. Misra, J. Levin, Rational orbits around charged black holes. Phys. Rev. D Part. Fields Gravit. Cosmol. **82**(8), 083001 (2010)
45. K. Glampedakis, D. Kennefick, Zoom and whirl: eccentric equatorial orbits around spinning black holes and their evolution under gravitational radiation reaction. Phys. Rev. D **66**(4), 044002 (2002)
46. L. Barack, C. Cutler, LISA capture sources: approximate waveforms, signal-to-noise ratios, and parameter estimation accuracy. Phys. Rev. D **69**(8), 082005 (2004)
47. R. Haas, Scalar self-force on eccentric geodesics in Schwarzschild spacetime: a time-domain computation. Phys. Rev. D **75**(12), 124011 (2007)
48. J. Healy, J. Levin, D. Shoemaker, Zoom-whirl orbits in black hole binaries. Phys. Rev. Lett. **103**(13), 131101 (2009)
49. J. Levin, G. Perez-Giz, A periodic table for black hole orbits. Phys. Rev. D **77**(10), 103005 (2008)
50. J. Levin, Energy level diagrams for black hole orbits. Class. Quantum Gravity **26**(23), 235010 (2009)
51. J. Levin, G. Perez-Giz, Homoclinic orbits around spinning black holes. I. Exact solution for the Kerr separatrix. Phys. Rev. D **79**(12), 124013 (2009)
52. G. Perez-Giz, J. Levin, Homoclinic orbits around spinning black holes. II. The phase space portrait. Phys. Rev. D **79**(12), 124014 (2009)
53. R. Grossman, J. Levin, G. Perez-Giz, Harmonic structure of generic Kerr orbits. Phys. Rev. D **85**(2), 023012 (2012)
54. R. Grossman, J. Levin, G. Perez-Giz, Faster computation of adiabatic extreme mass-ratio inspirals using resonances. Phys. Rev. D **88**(2), 023002 (2013)
55. C.-Q. Liu, C.-K. Ding, J.-L. Jing, Periodic orbits around Kerr Sen black holes. Commun. Theor. Phys. **71**(12), 1461 (2019)
56. S. Haroon, T. Zhu, Periodic orbits and their gravitational wave radiations in a black hole with a dark matter halo. Phys. Rev. D **112**(4), 044046 (2025)
57. M. Alloqulov, T. Xamidov, S. Shaymatov, B. Ahmedov, Gravitational waveforms from periodic orbits around a Schwarzschild black hole embedded in a Dehnen-type dark matter halo (2025). arXiv preprint arXiv:2504.05236
58. V. Misra, J. Levin, Rational orbits around charged black holes. Phys. Rev. D **82**(8), 083001 (2010)
59. G.Z. Babar, A.Z. Babar, Y.K. Lim, Periodic orbits around a spherically symmetric naked singularity. Phys. Rev. D **96**(8), 084052 (2017)
60. S.-W. Wei, J. Yang, Y.-X. Liu, Geodesics and periodic orbits in Kehagias–Sfetsos black holes in deformed Horava–Lifshitz gravity. Phys. Rev. D **99**(10), 104016 (2019)
61. B. Gao, X.-M. Deng, Bound orbits around Bardeen black holes. Ann. Phys. **418**, 168194 (2020)
62. X.-M. Deng, Periodic orbits around brane-world black holes. Eur. Phys. J. C **80**(6), 489 (2020)
63. X.-M. Deng, Geodesics and periodic orbits around quantum-corrected black holes. Phys. Dark Univ. **30**, 100629 (2020)
64. T.-Y. Zhou, Y. Xie, Precessing and periodic motions around a black-bounce/traversable wormhole. Eur. Phys. J. C **80**(11), 1070 (2020)
65. H.-Y. Lin, X.-M. Deng, Rational orbits around 4 D Einstein–Lovelock black holes. Phys. Dark Univ. **31**, 100745 (2021)
66. L. Meng, X. Zhaoyi, M. Tang, Bound orbits and gravitational wave radiation around the hairy black hole. Eur. Phys. J. C **85**(3), 306 (2025)
67. Y.-Z. Li, X.-M. Kuang, Yu. Sang, Precessing and periodic timelike orbits and their potential applications in Einsteinian cubic gravity. Eur. Phys. J. C **84**(5), 529 (2024)
68. J. Chen, J. Yang, Periodic orbits and gravitational waveforms in quantum-corrected black hole spacetimes. Eur. Phys. J. C **85**(7), 1–13 (2025)
69. T. Ze-Yi, T. Zhu, A. Wang, Periodic orbits and their gravitational wave radiations in a polymer black hole in loop quantum gravity. Phys. Rev. D **108**(2), 024035 (2023)
70. S. Yang, Y.-P. Zhang, T. Zhu, L. Zhao, Y.-X. Liu, Gravitational waveforms from periodic orbits around a quantum-corrected black hole. J. Cosmol. Astropart. Phys. **2025**(01), 091 (2025)
71. H.-Y. Lin, X.-M. Deng, Precessing and periodic orbits around hairy black holes in Horndeski's theory. Eur. Phys. J. C **83**(4), 311 (2023)
72. H.-Y. Lin, X.-M. Deng, Dynamics of test particles around hairy black holes in Horndeski's theory. Ann. Phys. **455**, 169360 (2023)
73. O. Shabbir, M. Jamil, M. Azreg-Aïnou, Periodic orbits and their gravitational wave radiations around the Schwarzschild–Mog black hole. Phys. Dark Universe **47**, 101816 (2025)
74. L. Zhao, M. Tang, X. Zhaoyi, Periodic orbits and gravitational wave radiation in short hair black hole spacetimes for an extreme mass ratio system. Eur. Phys. J. C **85**(1), 36 (2025)
75. Z.C.S. Chan, Y.-K. Lim, Periodic orbits of neutral test particles in Reissner–Nordström naked singularities. Gen. Relativ. Gravit. **57**(2), 35 (2025)
76. J. Zhang, Y. Xie, Probing a black-bounce-Reissner–Nordström spacetime with precessing and periodic motion. Eur. Phys. J. C **82**(10), 854 (2022)
77. C.H. Wang, Y.P. Zhang, T. Zhu, S.W. Wei, A new type of multi-branch periodic orbits in dyonic black holes (2025). arXiv preprint arXiv:2508.20558
78. J.-T. Yao, X. Li, Closed orbits in axial symmetric Finslerian extension of a Schwarzschild black hole. Phys. Rev. D **108**(8), 084067 (2023)
79. Q. Qi, X.-M. Kuang, Y.-Z. Li, Yu. Sang, Timelike bound orbits and pericenter precession around black hole with conformally coupled scalar hair. Eur. Phys. J. C **84**(6), 645 (2024)
80. H. Jiang, M. Alloqulov, W. Qiang, S. Shaymatov, T. Zhu, Periodic orbits and plasma effects on gravitational weak lensing by self-dual black hole in loop quantum gravity. Phys. Dark Universe **46**, 101627 (2024)
81. S. Lu, T. Zhu, Gravitational radiations from periodic orbits around einstein-\ae {} ther black holes (2025). arXiv preprint arXiv:2505.00294
82. L. Huang, Probing holonomy corrected Schwarzschild black holes with precessing and periodic orbits. Phys. Rev. D **111**(8), 084038 (2025)
83. S. Zare, T. Zhu, L.M. Nieto, S. Lu, H. Hassanabadi, Probing regular black holes with sub-planckian curvature through periodic orbits and their gravitational wave radiation (2025). arXiv preprint arXiv:2510.05166

84. J. Levin, R. Grossman, Dynamics of black hole pairs. I. Periodic tables. Phys. Rev. D **79**(4), 043016 (2009)
85. R. Grossman, J. Levin, Dynamics of black hole pairs. II. Spherical orbits and the homoclinic limit of zoom-whirliness. Phys. Rev. D **79**(4), 043017 (2009)
86. A. Kar, S. Kar, Diverse regular spacetimes using a parametrised density profile (2025). arXiv preprint arXiv:2504.12042
87. I. King, The structure of star clusters. i. an empirical density law. Astron. J. **67**, 471 (1962)
88. S.W. Hawking, Black hole explosions? Nature **248**(5443), 30–31 (1974)
89. S. Zare, F. Hosseinifar, L.M. Nieto, D.J. Gogoi, K. Boshkayev, A. Urazalina, H. Hassanabadi, Accretion disk luminosity and topological characteristics for a Schwarzschild black hole surrounded by king dark matter halo (2025). arXiv preprint arXiv:2510.03925
90. F. Gray, S. Schuster, A. Van-Brunt, M. Visser, The hawking cascade from a black hole is extremely sparse. Class. Quantum Gravity **33**(11), 115003 (2016)
91. A. Chowdhury, N. Banerjee, Greybody factor and sparsity of hawking radiation from a charged spherical black hole with scalar hair. Phys. Lett. B **805**, 135417 (2020)
92. Y. Sekhmani, S. Zare, L.M. Nieto, H. Hassanabadi, K. Boshkayev, Black holes immersed in polytropic scalar field gas. J. High Energy Astrophys. **47**, 100389 (2025)
93. G.W. Gibbons, The Jacobi metric for timelike geodesics in static spacetimes. Class. Quantum Gravity **33**(2), 025004 (2015)
94. S. Schneider, V. Perlick, The shadow of a collapsing dark star. Gen. Relativ. Gravit. **50**(6), 58 (2018)
95. Z.-L. Wang, E. Battista, Dynamical features and shadows of quantum Schwarzschild black hole in effective field theories of gravity. Eur. Phys. J. C **85**(3), 1–31 (2025)
96. M. Heydari-Fard, M. Heydari-Fard, H.R. Sepangi, Null geodesics and shadow of hairy black holes in Einstein–Maxwell-dilaton gravity. Phys. Rev. D **105**(12), 124009 (2022)
97. X.-X. Zeng, H.-Q. Zhang, Influence of quintessence dark energy on the shadow of black hole. Eur. Phys. J. C **80**(11), 1058 (2020)
98. K.S. Virbhadra, G.F.R. Ellis, Schwarzschild black hole lensing. Phys. Rev. D **62**(8), 084003 (2000)
99. R.A. Konoplya, Shadow of a black hole surrounded by dark matter. Phys. Lett. B **795**, 1–6 (2019)
100. A. Abdujabbarov, M. Amir, B. Ahmedov, S.G. Ghosh, Shadow of rotating regular black holes. Phys. Rev. D **93**(10), 104004 (2016)
101. B. Mashhoon, Scattering of electromagnetic radiation from a black hole. Phys. Rev. D **7**(10), 2807 (1973)
102. T. Regge, J.A. Wheeler, Stability of a Schwarzschild singularity. Phys. Rev. **108**(4), 1063 (1957)
103. M. Bouhmadi-López, S. Brahma, C.-Y. Chen, P. Chen, D. Yeom, A consistent model of non-singular Schwarzschild black hole in loop quantum gravity and its quasinormal modes. J. Cosmol. Astropart. Phys. **2020**(07), 066 (2020)
104. V. Ferrari, B. Mashhoon, New approach to the quasinormal modes of a black hole. Phys. Rev. D **30**(2), 295 (1984)
105. H.-J. Blome, B. Mashhoon, Quasi-normal oscillations of a Schwarzschild black hole. Phys. Lett. A **100**(5), 231–234 (1984)
106. S. Iyer, C.M. Will, Black-hole normal modes: a wkb approach. i. foundations and application of a higher-order wkb analysis of potential-barrier scattering. Phys. Rev. D **35**(12), 3621 (1987)
107. R.A. Konoplya, Quasinormal behavior of the d-dimensional Schwarzschild black hole and the higher order wkb approach. Phys. Rev. D **68**(2), 024018 (2003)
108. J. Matyjasek, M. Telecka, Quasinormal modes of black holes. ii. Padé summation of the higher-order wkb terms. Phys. Rev. D **100**(12), 124006 (2019)
109. R.A. Konoplya, A. Zhidenko, Quasinormal modes of black holes: from astrophysics to string theory. Rev. Mod. Phys. **83**(3), 793–836 (2011)
110. D.J. Gogoi, U.D. Goswami, Quasinormal modes of black holes with non-linear-electrodynamic sources in Rastall gravity. Phys. Dark Universe **33**, 100860 (2021)
111. Dhruba Jyoti Gogoi and Supakchai Ponglertsakul, Constraints on quasinormal modes from black hole shadows in regular non-minimal Einstein Yang–Mills gravity. Eur. Phys. J. C **84**(6), 652 (2024)
112. Dhruba Jyoti Gogoi, Violation of Hod's conjecture and probing it with optical properties of a 5-d black hole in Einstein gauss-bonnet bumblebee theory of gravity. Phys. Dark Universe **45**, 101535 (2024)
113. D.J. Gogoi, N. Heidari, J. Kříž, H. Hassanabadi, Quasinormal modes and greybody factors of de sitter black holes surrounded by quintessence in Rastall gravity. Fortschr. Phys. **72**(3), 2300245 (2024)
114. F. Hosseinifar, S. Mamedov, F. Studnička, H. Hassanabadi, Quasinormal modes and topological characteristics of a Schwarzschild black hole surrounded by the Dehnen type dark matter halo. Eur. Phys. J. C **85**(8), 819 (2025)
115. J. Matyjasek, M. Opala, Quasinormal modes of black holes. The improved semianalytic approach. Phys. Rev. D **96**(2), 024011 (2017)
116. R.A. Konoplya, Quasinormal modes of the Schwarzschild black hole and higher order WKB approach. J. Phys. Stud. **8**, 93–100 (2004)
117. A.F. Zinhailo, Quasinormal modes of Dirac field in the Einstein–Dilaton–Gauss–Bonnet and Einstein–Weyl gravities. Eur. Phys. J. C **79**(11), 912 (2019)
118. C. Gundlach, R.H. Price, J. Pullin, Late-time behavior of stellar collapse and explosions. ii. nonlinear evolution. Phys. Rev. D **49**(2), 890 (1994)
119. Z. Zhu, S.J. Zhang, C.E. Pellicer, B. Wang, E. Abdalla, Stability of Reissner–Nordström black hole in de sitter background under charged scalar perturbation. Phys. Rev. D **90**(4), 044042 (2014)
120. J. Maldacena, A. Strominger, Black hole greybody factors and d-brane spectroscopy. Phys. Rev. D **55**(2), 861 (1997)
121. I.R. Klebanov, S.D. Mathur, Black hole greybody factors and absorption of scalars by effective strings. Nucl. Phys. B **500**(1–3), 115–132 (1997)
122. M. Okyay, A. Övgün, Nonlinear electrodynamics effects on the black hole shadow, deflection angle, quasinormal modes and greybody factors. J. Cosmol. Astropart. Phys. **2022**(01), 009 (2022)
123. M. Visser, Some general bounds for one-dimensional scattering. Phys. Rev. A **59**(1), 427 (1999)
124. P. Boonserm, T. Ngampitipan, P. Wongjun, Greybody factor for black holes in drgt massive gravity. Eur. Phys. J. C **78**, 1–12 (2018)
125. V. Cardoso, M. Cavaglia, L. Gualtieri, Black hole particle emission in higher-dimensional spacetimes. Phys. Rev. Lett. **96**(7), 071301 (2006)
126. S.H. Dong, F. Hosseinifar, F. Studnička, W.S. Chung, H. Hassanabadi, Thermodynamic properties and topological charge of a static black hole in loop quantum gravity. Phys. Dark Universe 101962 (2025)
127. M. Cvetič, F. Larsen, Greybody factors for rotating black holes in four dimensions. Nucl. Phys. B **506**(1–2), 107–120 (1997)
128. Y. Décanini, G. Esposito-Farese, A. Folacci, Universality of high-energy absorption cross sections for black holes. Phys. Rev. D Part. Fields Gravit. Cosmol. **83**(4), 044032 (2011)